Supplementary information

Harnessing pseudoelasticity in SMA-based negative stiffness mechanical metamaterials for superior strength and recoverability

Xianhua Yao[a], Liangyu Huang[b], Jiale Cheng[b], Jiachen Li[b], Yiwei Yin[b], Yifan Wang[c], Xiaohu Yao[a,b], Nan Hu[a,b]*

[a] State Key Laboratory of Subtropical Building and Urban Science, Guangzhou 510641, China

[b] School of Civil Engineering and Transportation, South China University of Technology, Guangzhou, 510641, China

[c] School of Mechanical and Aerospace Engineering, Nanyang Technological University, Singapore 639798, Singapore

*Corresponding author: Prof. Nan Hu (nanhu026@scut.edu.cn)

The file includes:

Supplementary Note 1-2

Supplementary Figure 1-9

Supplementary Table 1-7

Supplementary Note 1. Material property of NiTi SMA

To evaluate the cyclic tensile constitutive behavior of the NiTi shape memory alloy (SMA) used in this study, dog-bone-shaped specimens were machined from the same NiTi plate employed for fabricating the negative stiffness curved beam specimens. The specimens had a rectangular cross section of 6 mm × 2 mm, as shown in Fig. S1(a). Incremental cyclic tensile tests were performed under displacement-controlled loading with a constant rate of ^{1} mm/min. The strain amplitudes of the cyclic loading were successively set to 1%, 2%, 3%, 4%, 5%, and 6%. Both loading and unloading were conducted at the same rate, and unloading was terminated when the measured force returned to zero. The loading protocol is illustrated in Fig. S1(b). Fig. S1(c) presents representative cyclic stress–strain curves of the pseudoelastic NiTi SMA. The results show that the apparent "yield" stress during loading is approximately $\sigma_{MS} = 440$ MPa, corresponding to the onset of the stress-induced martensitic transformation. The transformation is nearly complete at a strain of 5%, with a corresponding stress of $\sigma_{MF} = 540$ MPa. As the number of cycles increases, the residual strain accumulates progressively, from about 0.015% after the 1% strain cycle to 0.59% after the 5% strain cycle, mainly due to local slip events occurring during the martensitic transformation. The experimentally determined material properties of the SMA are summarized in Table S1, which are subsequently used in the numerical simulations of the negative stiffness curved beam energy-dissipating structures.

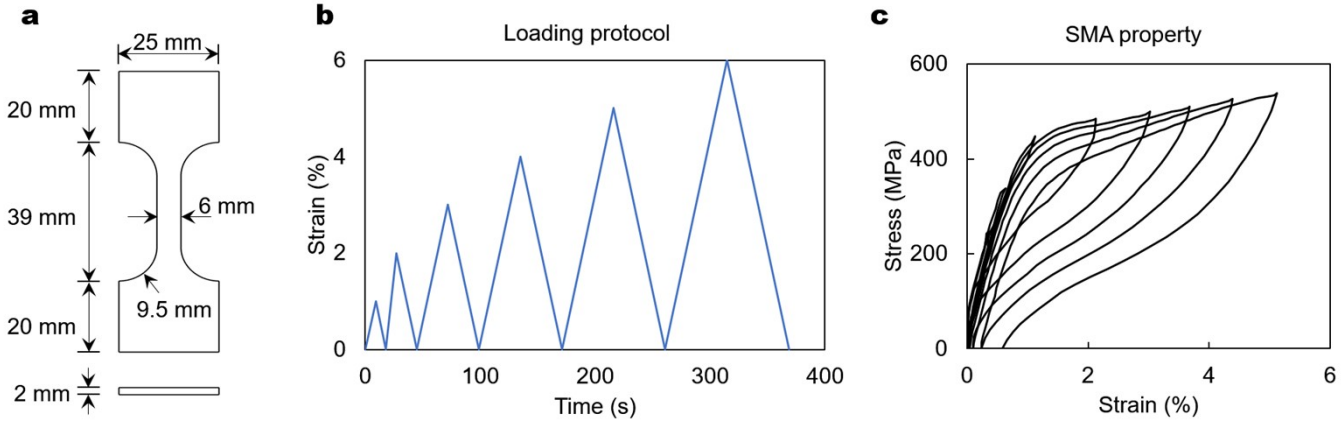

Fig. S1. Mechanical properties of NiTi shape memory alloy material. (a) Geometric parameters of dog-bone specimen. (b) Loading protocol. (c) Tested stress-strain curves.

Table S1 Material parameters for the SMA material

E_A	E_M	σ_{MS}	ε_{MS}	σ_{MF}	ε_{MF}	σ_{AS}	σ_{AF}	ε_t	ν
44 GPa	18 Gpa	440 MPa	0.01	540 MPa	0.051	250 MPa	150 MPa	0.021	0.3

Supplementary Note 2. Theoretical analysis for SMA-based negative stiffness metamaterial

Based on the force–displacement response of negative stiffness curved beam unit, the stable equilibrium paths of the corresponding curved beam array structure can be determined through model analysis. This approach enables a quantitative evaluation of the overall force–displacement behavior and the energy-dissipation performance of an array consisting of n curved beams connected in series. Conventional model analysis method is applicable when the loading and unloading force–displacement paths of curved beam unit are identical, as typically observed in elastic or hyperelastic systems.

However, for negative stiffness curved beams made of shape memory alloy (SMA), the intrinsic hysteretic behavior caused by the phase transformation of the SMA material leads to non-coincident loading and unloading curves. Therefore, it is necessary to separately obtain the loading and unloading equilibrium paths of the array structure based on the corresponding unit force–displacement responses. As illustrated in Fig. S2, the force–displacement curve of the SMA-based curved beam unit is decomposed into loading and unloading segments. Using the analytical model developed in previous study, two stable equilibrium paths of the SMA curved beam array are determined independently for loading and unloading. The outer envelope of these two equilibrium paths then represents the overall force–displacement response of the SMA-based negative stiffness curved beam array with a given number of serially connected units.

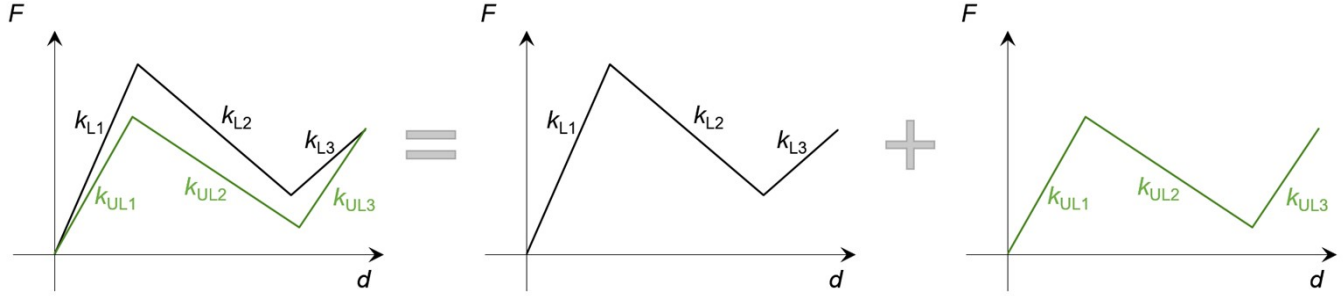

Fig. S2. The illustration of the force-displacement response of SMA NS curved beam element.

Taking the unit with geometric parameters $h = 2$ mm, $t = 1$ mm, $L = 40$ mm and $b = 10$ mm as an example, the loading and unloading force–displacement responses of a single unit were first obtained by numerical simulation. Each of the two hysteretic branches (loading and unloading) is then approximated by a piecewise polynomial fit to simplify subsequent array-level analysis. Specifically, the loading path is decomposed into three segments represented by polynomials k_{L1}, $k_{L2}$and k_{L3}, and the unloading path is decomposed similarly into k_{UL1}, $k_{UL2}$and k_{UL3}. The three segments correspond to an initial response approximated by a cubic polynomial, a negative-stiffness segment approximated linearly, and a third

segment approximated by a quadratic polynomial. The piecewise representations for the loading (F_L) and unloading (F_{UL}) curves are written as

$$F_{Li} = [k_{Li}]D_{Li} \tag{S1}$$

$$F_{ULi} = [k_{ULi}]D_{ULi} \tag{S2}$$

$$F_{Li} = \begin{cases} a_{1_L}D_i^3 + b_{1_L}D_i^2 + c_{1_L}D_i + d_{1_L} & 0 \le D_i \le d_{top} \\ a_{2_L}D_i + b_{2_L} & d_{top} < D_i \le d_{bot} \\ a_{3_L}D_i^2 + b_{3_L}D_i + c_{3_L} & D_i > d_{bot} \end{cases} \tag{S3}$$

$$F_{ULi} = \begin{cases} a_{1_{UL}}D_i^3 + b_{1_{UL}}D_i^2 + c_{1_{UL}}D_i + d_{1_{UL}} & 0 \le D_i \le d_{top} \\ a_{2_{UL}}D_i + b_{2_{UL}} & d_{top} < D_i \le d_{bot} \\ a_{3_{UL}}D_i^2 + b_{3_{UL}}D_i + c_{3_{UL}} & D_i > d_{bot} \end{cases} \tag{S4}$$

where D is the displacement of beam element, k_{Li} and k_{ULi} is the equivalent stiffness of curved beam element that is in regimes 1, 2 and 3 in loading and unloading path, respectively. The coefficients *a*, *b*, c, and *d* for each regime can be obtained by fitting the force-displacement relation predicted by FE analysis. And the fitted coefficients are summarized in Table. S2.

Table S2 Coefficient of simplified loading and unloading force-displacement curves

	a_1	b_1	c_1	d_1	a_2	b_2	a_3	b_3	c_3
Loading	0	-31.918	63.714	0	-12.397	44.397	15.918	-96.368	153.15
Unloading	30.187	-77.915	70.094	0	-9.1224	30.139	27.428	-171.88	271.1

As for a beam chain containing *n* beams connected in series, when the chain system is subjected to a vertical load, assuming that just one complete row of curved beams is transitioning to the second stable configuration at a time, we can relate the behavior of a single beam element with the global mechanical behavior of the chain system. Hence, the global force-displacement response of beam chain representing the stable equilibrium path with snap-back behavior in loading and unloading path can be obtained by solving following equations:

$$D = n_1D_1(F) + n_2D_2(F) + n_3D_3(F) = \sum_{i=1}^{n_1} k_{i1}^{-1}(F_1) + n_2k_{i2}^{-1}(F_2) + \sum_{i=1}^{n_3} k_{i3}^{-1}(F_3) \tag{S5}$$

$$F = F_i \tag{S6}$$

$$F_{bot} \le F \le F_{top} \tag{S7}$$

where $D_i(F)$ corresponds to the displacement for a beam element in a particular regime measured with respect to its undeformed configuration and can be derived from Eq. S1 and S2. k_{i1}^{-1}, k_{i2}^{-1}, and k_{i3}^{-1} are the inverse functions of Eq. S3 and S4. The black dash–dot line in Fig. S3 (a) and (b) is the theoretical force-

displacement response of beam chain in loading and unloading path. Under displacement-controlled loading and unloading, the actual force-displacement curves is identified by the blue and yellow solid lines, resulting in the final response of 4×2 SMA NS curved beam structure, shown in Fig. S3(c).

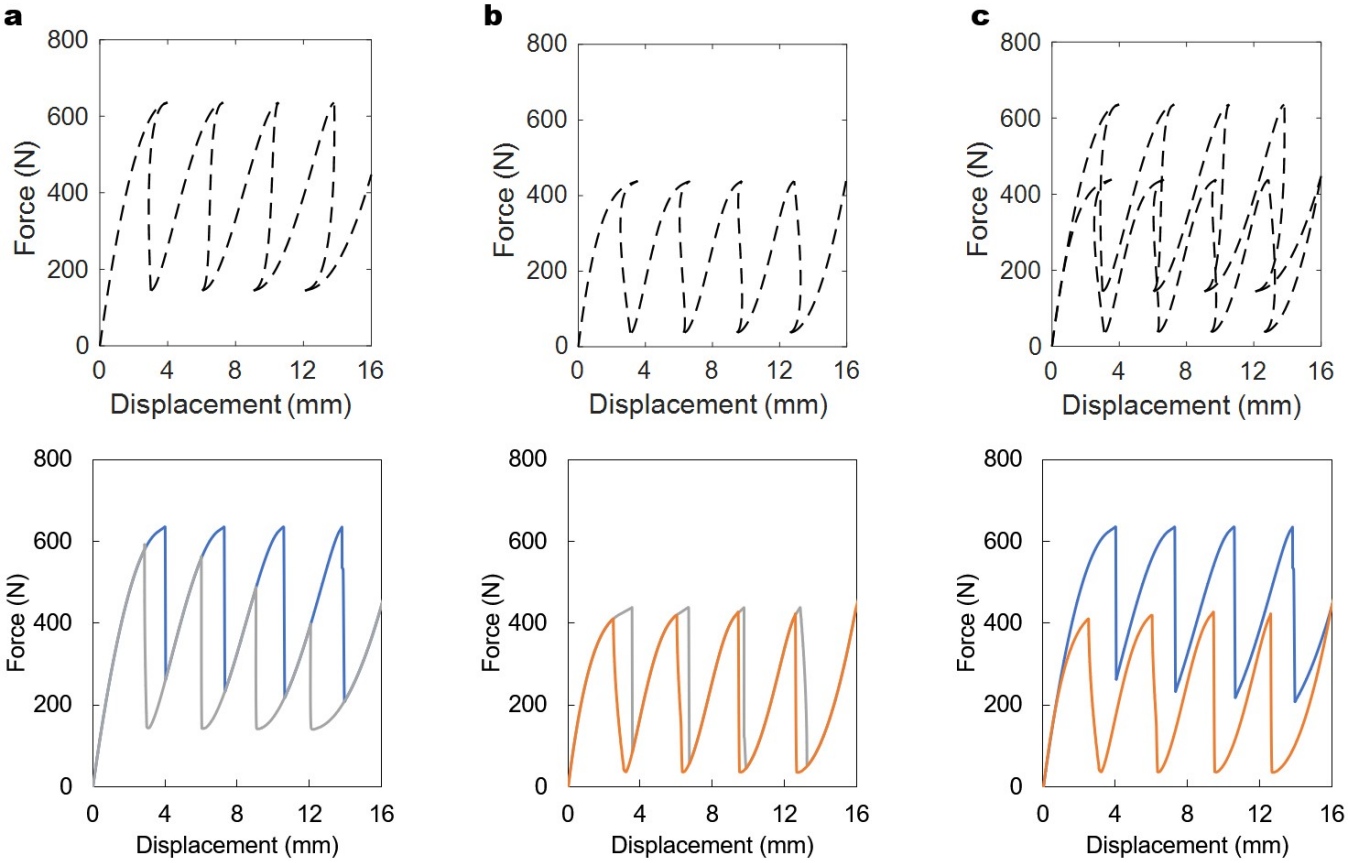

Fig. S3. Equilibrium path and analyzed force-displacement curves of 4×2 SMA NS curved beam structure. (a) Loading path. (b) Unloading path. (c) Loading-unloading path.

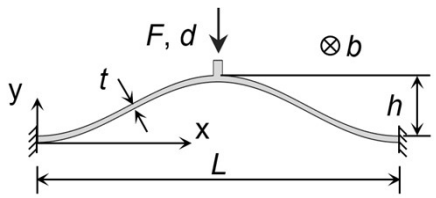

Fig. S4. Geometric parameters of the curved beam unit.

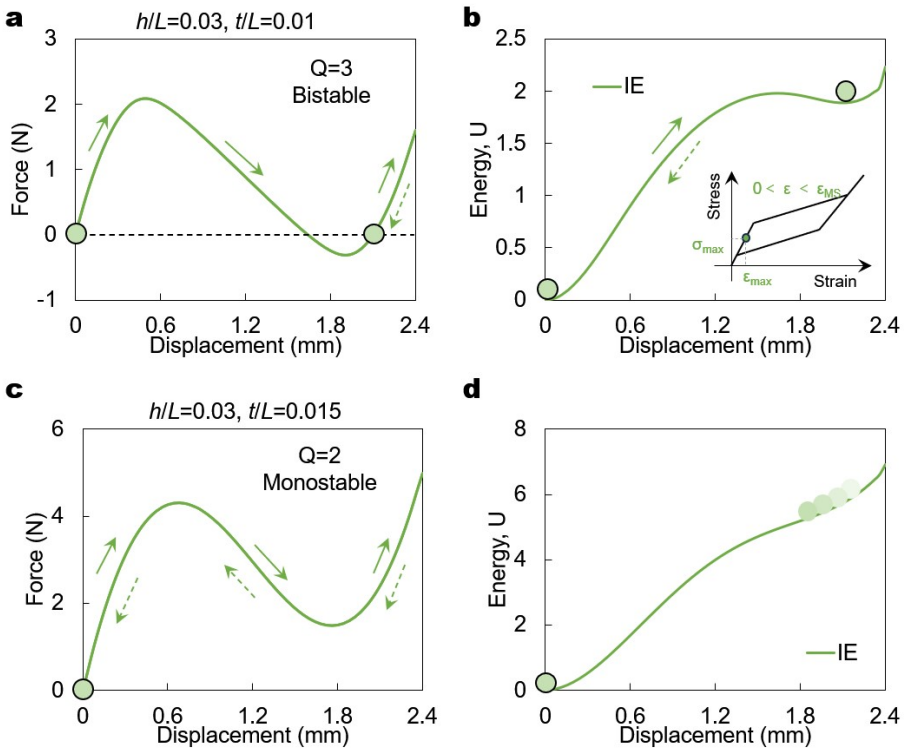

Fig. S5. Mechanical response of the SMA curved beam unit in elastic regime. (a) and (c) Force-displacement curves of curved beam units with Q = 3 and Q = 2. (b) and (d) Variation of potential energy for curved beam with Q = 3 and Q = 2 during the loading–unloading process.

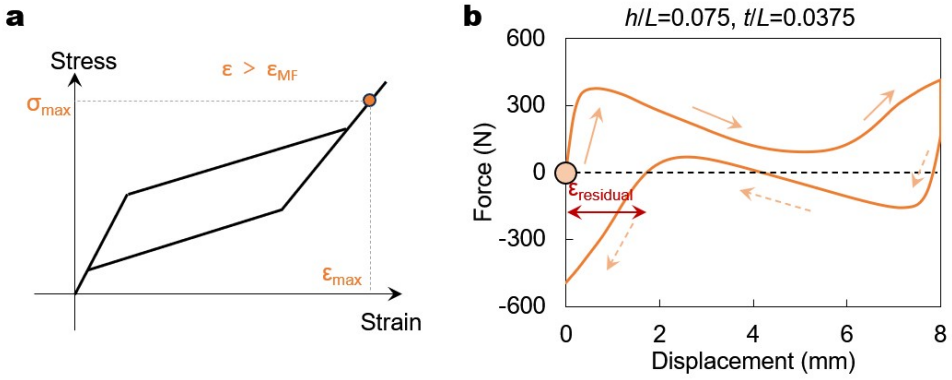

Fig. S6. Mechanical response of the SMA curved beam unit in plastic regime. (a) The strain level of curved beam during deformation in SMA base material. (b) Force-displacement curves of curved beam in plastic regime.

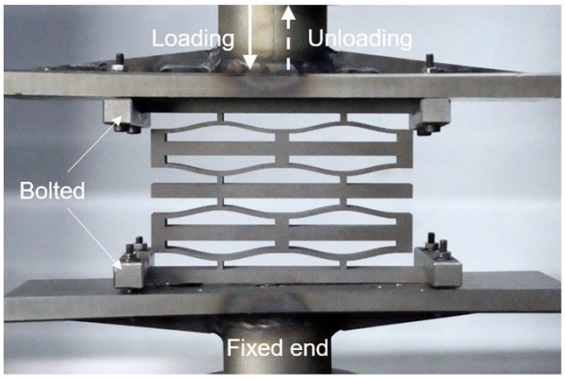

Fig. S7. Experimental set-up.

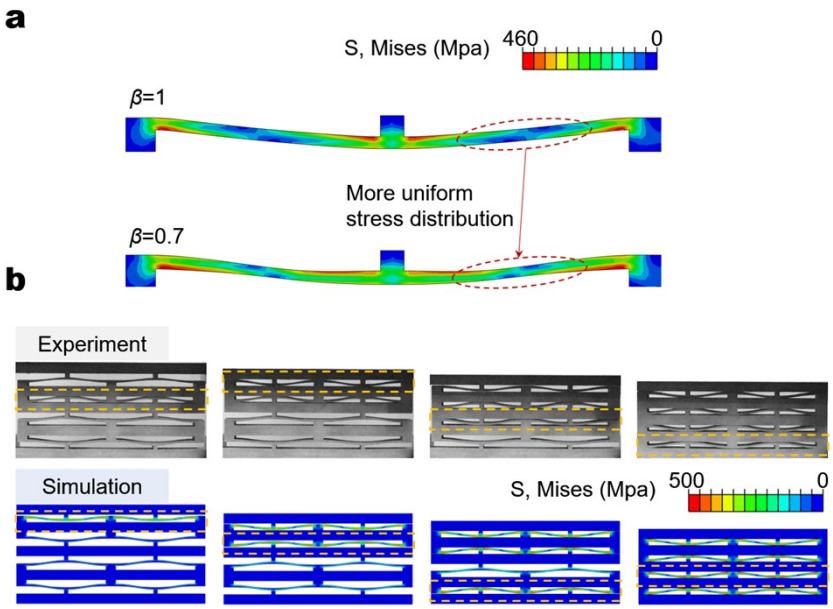

Fig. S8. Stress distribution and deformation process of SMA curved beam metamaterial with non-uniform thickness design. (a) Comparison of stress distribution of curved beam unit with β=0.7 and β=1. (b) Deformation process of 4×2 SMA curved beam metamaterial with β=0.7.

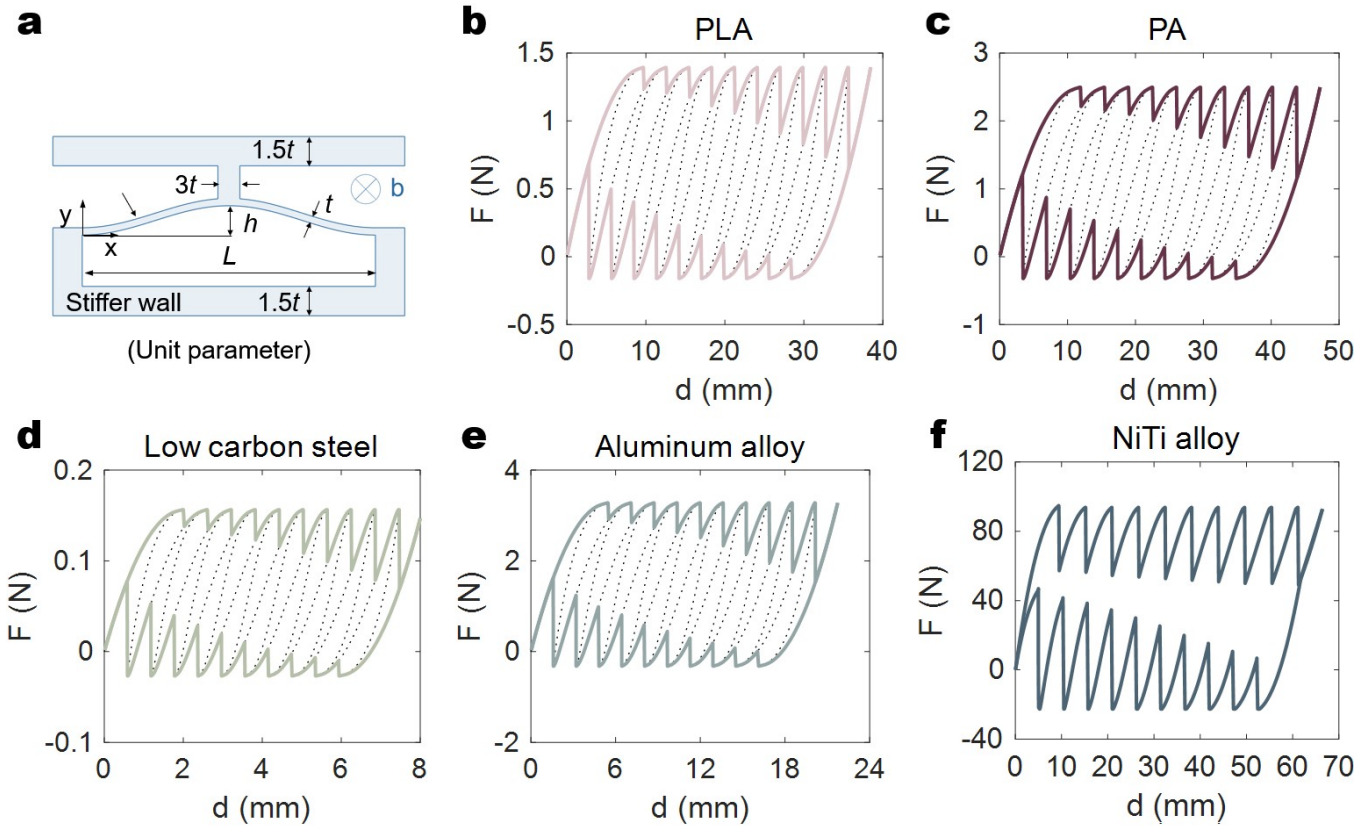

Fig. S9. The force-displacement responses of 10×1 SMA curved beam structures with different base material. (a) Unit parameters. (b) PLA. (c) PA. (d) Low carbon steel. (e) Aluminum alloy. (f) NiTi alloy.

Table S3 Geometry parameters of various array structures and corresponding mass

No.	n	m	h (mm)	t (mm)	b (mm)	L (mm)	β	Q	$\varepsilon_{max\_designed}$ (%)	Strain phase	Mass (g)
1	4	2	2	1	10	40	1	2	3.29	$\varepsilon_{MS} < \varepsilon < \varepsilon_{Mf}$	204.8
2	4	2	3	1	10	40	1	3	4.52	$\varepsilon_{MS} < \varepsilon < \varepsilon_{Mf}$	210
3	4	2	3	1.5	10	40	1	2	7.40	$\varepsilon > \varepsilon_{Mf}$	222.5
4	4	2	2	1	10	40	0.7	2	-	$\varepsilon_{MS} < \varepsilon < \varepsilon_{Mf}$	205.7

Table S4 Metal and polymer base material properties

Base material		E/Gpa	σ_y/Mpa	ε_y	ρ/g/cm3
Metal	Stainless steel	190	200	0.00116	8
	Low carbon steel	200	200	0.00125	7.85

	Aluminum alloy	71	465	0.00711	2.81
	Titanium alloy	110	850	0.00818	4.43
	NiTi alloy	75	195	0.06	6.45
	PLA	3.2	60	0.02188	1.43
	ABS	2.1	45	0.02619	1.03
Polymer	PP	1.3	32	0.02923	0.90
	PEEK	3.5	90	0.03143	1.28
	PA	2.6	70	0.03269	1.2

Table S5 Geometry parameters of five curved beam negative stiffness metamaterials with various based materials

	Material	t/mm	h/mm	b/mm	L/mm	Q	ε_{max}
	Low carbon steel	0.15	0.39	1.00	40.00	2.5	0.00094
Metal	Aluminum alloy	0.43	1.06	1.00	40.00	2.5	0.007076
	NiTi alloy	1.24	3.09	1.00	40.00	2.5	0.059683
Ploymer	PLA	0.75	1.87	1.00	40.00	2.5	0.021788
	PA	0.91	2.29	1.00	40.00	2.5	0.032693

Table S6. Recoverability and strength Ashby plot data

Reference	Name	Strength (MPa)	Recoverability
This work	SMA-NS-metamaterial	0.793	1
This work	SMA-NS-metamaterial	1.415	1
This work	SMA-NS-metamaterial	2.991	1
Restrepo et al. (2015)	PXCM	0.002	1
Zhang et al. (2019)	2D PXCM (T-type)	0.0422	1
Zhang et al. (2019)	2D PXCM (S-type)	0.0563	1
Chan et al. (2019)	Cubic lattice	0.0008	1
Lv et al. (2024)	NPR honeycomb	0.08	1
	Lamellar lattice (N=1)	0.287	0.64
	Lamellar lattice (N=2)	0.361	0.66
	Lamellar lattice (N=3)	0.313	0.76
Tian et al. (2024)	Lamellar lattice (K=1)	0.207	0.7
	Lamellar lattice (K=2)	0.3645	0.7
	Lamellar lattice (K=3)	0.0488	0.7
	Lamellar lattice (K=4)	0.0136	0.7
Schaedler et al. (2011)	Ni-P Microlattices	0.2	0.32
		0.4	0.32
Chen et al. (2021)	Gradient NS honeycomb	0.0095	1
Rachel et al. (2017)	Metallic glass nanolattice	0.2	0.52
Yan et al. (2025)	Snap-through metamaterial	0.35	1
Meza et al. (2015)	Hierarchical ceramic lattices	0.12	0.85
Shan et al. (2015)	Energy-trapping metamaterial	0.0025	1

		0.0065	1
Shi et al. (2021)	Multistable perforated shellular	0.008	1
		0.004	1
Frenzel et al. (2016)	Tailored Buckling microlattices	0.158	1
Frenzel et al. (2016)	Tailored Buckling microlattices	0.17	1
Li el al. (2024)	CFRP composite metamaterials	0.345	0.95
		3.225	0.9
Li et al. (2024)	3D tiled auxetic metamaterial	0.25	0.9
Zheng et al. (2016)	Nickel alloy hierarchical metamaterial	0.13	0.85
Rafsanjani et al. (2015)	Snapping mechanical metamaterials	0.11	1

Table S7. Specific energy dissipation and strength Ashby plot data

Reference	Name	Strength (MPa)	Specific energy dissipation (SED) (J/kg)
This work (EXP)	SMA NS metamaterial	0.793	7.793
	SMA NS metamaterial	1.415	23.883
	SMA NS metamaterial	2.991	58.647
This work (FEM)	SMA NS metamaterial	0.463	186.454
		1.966	476.707
		2.371	263.268
		1.459	22.175
		0.037	39.449
		1.975	4.181
		2.375	5.66
		1.463	1.452
		1.983	480.617
		2.388	260.556
		1.464	22.267
Rafsanjani et al. (2015)	Snapping mechanical metamaterials	0.11	8.8
Li el al. (2024)	CFRP composite metamaterials	0.345	350
Li el al. (2024)	CFRP composite metamaterials	0.021	140
Shi et al. (2021)	Multistable perforated shellular	0.0065	0.64
Shi et al. (2021)	Multistable perforated shellular	0.008	1.032
Shi et al. (2021)	Multistable perforated shellular	0.004	0.0576
Frenzel et al. (2016)	Tailored Buckling Microlattices	0.158	150
Haghpanah et al. (2016)	Shape-reconfigurable materials	0.2	120
Li et al. (2024)	3D tiled auxetic metamaterial	0.25	2.7
Ma et al. (2022)	Tri-directional metastructure	0.06	15
Yan et al. (2025)	Snap-through metamaterial	0.35	8.94
Chen et al. (2020)	Composite NS structure	0.045	8.5
Chen et al. (2021)	Gradient NS honeycomb	0.0095	20.26
Fu et al. (2019)	Granular metamaterials	0.0041	2.5
Itamar et al. (2020)	Shallow dome FSM	0.006	2.35
Lv et al. (2024)	NPR honeycomb	0.08	33.3
Chan et al. (2019)	Cubic lattice	0.0008	2.63
Zhang et al. (2019)	T-type PXCM	0.0422	9.21
Zhang et al. (2019)	S-type PXCM	0.0563	10.42